

Electric transport as a probe to unveil microscopic aspects of oxygen-depleted YBCO

C. Acha,^{1,*} A. Camjayi,¹ T. Vaimala,² H. Huhtinen,² and P. Paturi²

¹*Universidad de Buenos Aires, Facultad de Ciencias Exactas y Naturales, Departamento de Física, Laboratorio de Bajas Temperaturas and IFIBA, UBA-CONICET, Pabellón I, Ciudad Universitaria, C1428EHA CABA, Argentina*

²*University of Turku, Department of Physics and Astronomy, Wihuri Physical Laboratory, FI-20014 Turku, Finland*

(Dated: January 28, 2025)

Abstract

We report on the characterization of Pt-YBa₂Cu₃O_{7- δ} interfaces, focusing on how oxygen vacancies content (δ) affects electrical transport mechanisms. Our study examines four Pt-YBa₂Cu₃O_{7- δ} samples with varying δ ($0.12 \leq \delta \leq 0.56$) using voltage-current measurements across a temperature range. We successfully model the electrical behavior using a Poole-Frenkel conduction framework, revealing that oxygen vacancies create potential wells that trap carriers, directly influencing conduction. We observe that the energy of these traps increases as δ rises, in agreement with a peak previously detected in optical conductivity measurements. This result supports earlier interpretations, strengthening the proposed connection between oxygen vacancies and the ionization energy associated with impurity bands in oxygen-depleted YBa₂Cu₃O_{7- δ} .

PACS numbers: 73.40.-c, 66.30.-h, 74.72.-h

I. INTRODUCTION

The $\text{YBa}_2\text{Cu}_3\text{O}_{7-\delta}$ (YBCO) superconductor has garnered substantial attention for numerous years, due to its pivotal role in defining the landscape of high-temperature superconductors, captivating scientific and technological interest. Its high-temperature superconducting capabilities have spurred extensive investigations to unravel the intricate mechanisms governing its unique properties.¹ One of the key enigmas lies in the role of oxygen stoichiometry, diffusion and ordering, all critical parameters influencing both normal-state and superconducting behaviors, being also factors dictating the diverse phases observed in YBCO. Its understanding holds implications not only for YBCO but also for a broad spectrum of oxide materials and their derived applications. Seminal neutron diffraction studies on oxygen-depleted $\text{YBCO}_{7-\delta}$ samples exhibiting diverse δ values², have elucidated that oxygen vacancies are mainly located at the O position in the CuO chains (O(1) sites, following ref.² notation), along the crystallographic b-axis, establishing a diffusion channel with minimal impediments.

On a different note, a remarkable progress has already been achieved in comprehending the physics associated with the mechanisms governing the write and retention processes in resistive memories, particularly those linked to oxides where oxygen migration triggers resistive switching (RS).³ This is evident in devices based on transition metal oxides, like TiO_2 , Ta_2O_5 , manganites, cobaltites, and superconducting cuprates, among other materials. Devices based on metal- $\text{YBCO}_{7-\delta}$ may not find widespread application in memory mainstream technology due to integration challenges with Si-based electronics and their partial retentivity⁴, attributed to high oxygen diffusivity in specific crystallographic directions⁵. Nevertheless, their significance lies in unveiling the electrical transport mechanisms through a metal-complex oxide interface, a recurring characteristic in many memristive interfaces. Remarkably, non-recting metal (Au, Pt)-YBCO interfaces have demonstrated interesting bipolar resistive switching properties⁶⁻¹⁰, coupled with distinctive relaxation effects^{5,11}, electrochemical control of YBCO's carrier density¹² and its superconducting performance¹³, and peculiar characteristics associated with inhomogeneous interfaces^{4,14-18}. Particularly, the description of its electrical properties has been achieved through an equivalent circuit that considers the Poole-Frenkel (PF) mechanism as responsible for its non-linear conduction (see Fig. 1).

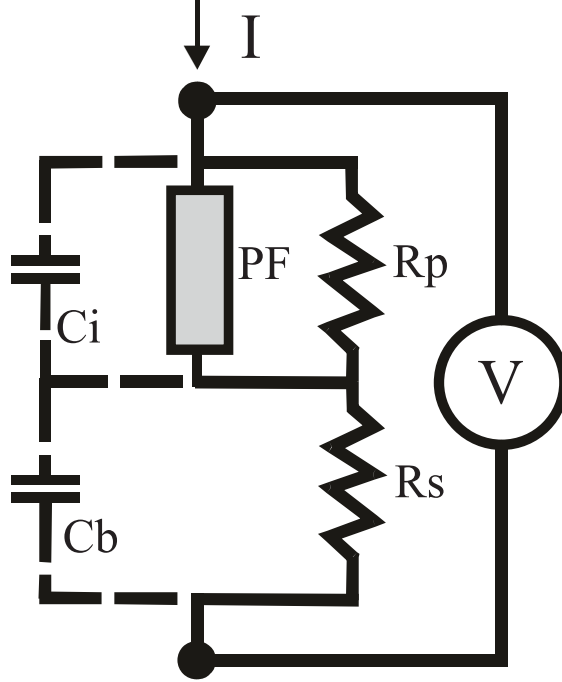


FIG. 1: Equivalent circuit model for the metal-transition metal oxide interface. A Poole-Frenkel (PF) type conduction is presented here as the particular non-linear mechanism. R_p and R_s are the parallel and series resistors, respectively (see text). The capacitances C_i (interfacial) and C_b (bulk) only have a relevant role when operating with alternating current at moderate to high frequencies.

It should be noted that neither Au nor Pt cause chemical reactions or ion migration in YBCO. However, they influence the electronic levels through the alignment of the Fermi energies of the metal and the oxide, creating an interfacial region (or depletion layer) with electronic properties distinct from the bulk but still indicative of the oxide's intrinsic characteristics.¹⁹ The equivalent circuit shown in Fig. 1 also accounts for the distinction of interfacial and bulk regions. The parallel combination of R_p (ohmic) and R_{PF} (the non-linear resistor associated with PF emission) corresponds to the interfacial region. The bulk contribution is captured by the resistor R_s .

Under this description, one might consider that PF traps are solely associated with the interfacial region, with their origin potentially linked, for example, to surface defects. However, it would also be possible that these traps could also exist in the bulk, representing an intrinsic property of YBCO. In the circuitual description, they might not be considered because their effect in the bulk can be negligible, as the low bulk resistance (R_s) may effectively short-circuit their contribution. In contrast, the interfacial region, with a resistance (R_p)

comparable to R_{PF} , allows for their effects to be more readily observed. This sort of "amplification" effect of the intrinsic bulk oxide properties at the metal-oxide interface was also noted in a previous study of Au-YBCO interfaces.⁶ In that study, although the contact resistance was 100 times higher than the bulk resistance—which might suggest a YBCO insulating behavior—it actually exhibited metallic characteristics and demonstrated the superconducting resistive transition of YBCO. The resistance variation observed throughout the width of the transition was over an order of magnitude greater than that of bulk YBCO. Additionally, it is worth noting that non-linear IV characteristics were also observed in bulk (4W) measurements of highly deoxygenated YBCO sintered pellets²⁰ which are consistent with a scenario involving a combination of ohmic and PF-type conduction inherent to YBCO.¹⁴ Within this framework, we aim to elucidate the intrinsic characteristics of electrical transport in oxygen-depleted YBCO by measuring electrical transport across the Pt-YBCO_{7- δ} interface, where the oxygen content of YBCO has been systematically controlled. This approach aims to correlate the presence of PF traps with oxygen vacancies, enabling us to analyze their specific influence on electrical conduction and providing a unique opportunity to gain deeper insights into the role of these vacancies as carrier traps.

Here, we examine the electrical transport features of 4 Pt-YBCO_{7- δ} thin film interfaces. By intentionally varying YBCO's oxygen deficiency during the post-annealing vacuum treatment ($0.12 \leq \delta \leq 0.56$), our goal is to unravel the δ dependence of microscopic parameters linked to PF traps.

II. EXPERIMENTAL DETAILS

A series of superconducting YBCO thin films, ≈ 150 nm in thickness, were deposited using pulsed laser deposition (PLD) on (100) SrTiO₃ (STO) substrates. The film growth process utilized a 308 nm XeCl excimer laser with a pulse duration of 25 ns and a repetition rate of 5 Hz, delivering a laser fluence of 1.6 J/cm². The oxygen pressure within the deposition chamber was maintained at 0.2 torr, and the substrate temperature during deposition was set at 750 °C. To optimize the intrinsic film properties, *in situ* post-annealing treatments were conducted at a temperature of 725 °C in atmospheric pressure oxygen, employing heating and cooling rates of 25 °C/min. Further details regarding the PLD system, growth process, and deposition parameters can be found elsewhere in comprehensive reports²¹⁻²³.

The introduction of various oxygen deficiencies and subsequent variations in the critical temperatures of the samples² was accomplished by annealing the pristine samples in the pre-chamber of the electron beam evaporator. In this setup, adjustments could be made to the sample temperature, heat treatment time, and chamber pressure. The processing parameters for the final set of samples (labeled S1 to S4) included a constant chamber pressure of 1.0×10^{-7} mbar and pristine sample annealing temperatures of 350 °C (S1), 400 °C (S2), 425 °C (S3), and 475 °C (S4). The heating and cooling rates for these treatments were set at 10 °C/min, and the duration of each treatment at the target temperature was 60 s.

The ultimate oxygen deficiencies were determined by calculating the ratios of the x-ray diffraction (XRD) (005) and (004) peak intensities, denoted as $I(005)/I(004)$, as extensively detailed in ref.²⁴ (see details in the Supplementary Material section). The superconducting critical temperatures (T_c) were derived from the temperature-dependent susceptibilities, as depicted in the inset of Fig. 2. Here, T_c was determined using the criterion of 50% of χ , aligning closely with the first-order derivative of the susceptibility curve. The observed experimental relationship between critical temperature and oxygen deficiency is presented in Fig. 2, demonstrating a consistent alignment with the previously described dependence observed in oxygen-deficient YBCO powder samples².

In order to electrically characterize the Pt-YBCO_{7- δ} interfaces, several electrodes were deposited on top of each YBCO_{7- δ} thin film. This process involved employing photolithography and depositing high-purity Pt by sputtering technique. The resulting Pt-sputtered electrodes possess a narrow thickness of 30 nm, cover an area measuring 0.7 x 0.7 mm², and maintain a consistent separation of 0.4 mm. Subsequent to this fabrication, Pt leads were affixed using silver paint, ensuring a meticulous connection without direct contact with the YBCO sample surface (see Fig. 3).

To characterize the current-voltage (IV) response of the Pt/YBCO interfaces at different temperatures, 1 ms voltage pulses were applied between two Pt electrodes, labeled as "1" and "2" respectively, systematically cycling their amplitude using an Agilent B2902B SMU. Pulses were applied instead of a DC current to limit local Joule dissipation and thus minimize the possibility of RS occurrence, which could alter the oxygen vacancy distribution, primarily in the interfacial region where most of the applied voltage drops. The cycling involved varying the voltage between two extreme values, starting from the negative value and reaching the positive one in each cycle. The contact design was configured to facilitate

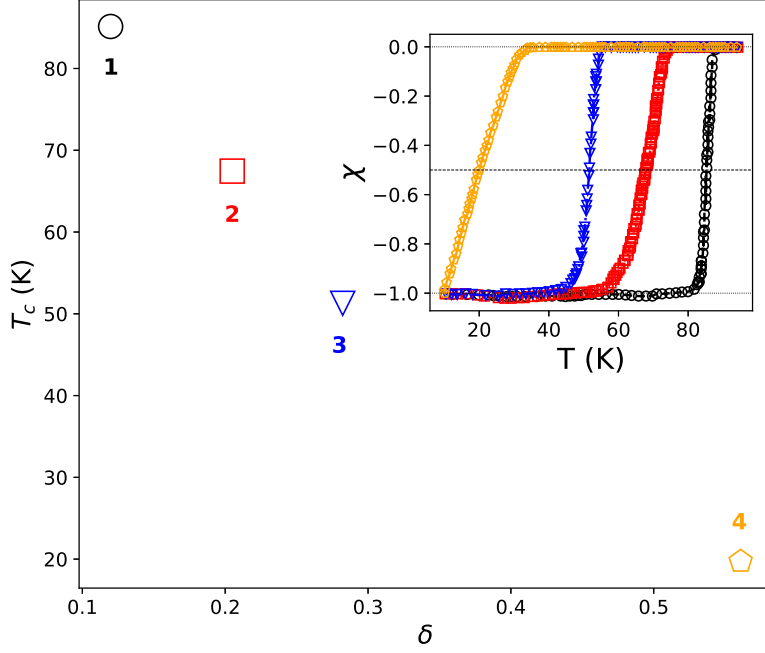


FIG. 2: Critical superconducting temperature (T_c , determined by the criterion of the 50% of the magnetic susceptibility χ transition, shown in the inset) as a function of the oxygen deficiency (δ), identified through the ratio between the 2θ (005) and (004) peaks from characterizations using XRD in each film. Next to each point, the numbers associated with each of the samples are indicated.

both 2-Wire (2W) and 3-Wire (3W) measurements by introducing an additional electrode ("3") between the aforementioned ones, allowing for a comprehensive characterization of each Pt/YBCO interface. Simultaneously, the instrument quantified the circulating current (I) throughout each pulse and measured the potential difference across the electrodes V_{1-2} (2W) and V_{1-3} (3W). Introducing a $V_{bias} = 0.1V$ pulse between each main pulse allowed us to measure the remnant resistance, denoted as R_{rem} . Each IV measurement was conducted with temperature stabilization better than 250 mK within the overall range of 80 K to 300 K, with steps ranging from 5 K to 10 K. It is worth noting that the lower limit of the measured temperature for each film was restricted to guarantee the execution of low-noise measurements, when the interface resistance becomes too large. In addition, the voltage range explored for each device was tailored to prevent a RS at any temperature. To achieve this, a 'safe' voltage range was initially used to obtain IV characteristics for all studied temperatures. The range was gradually extended, repeating the study for all temperatures

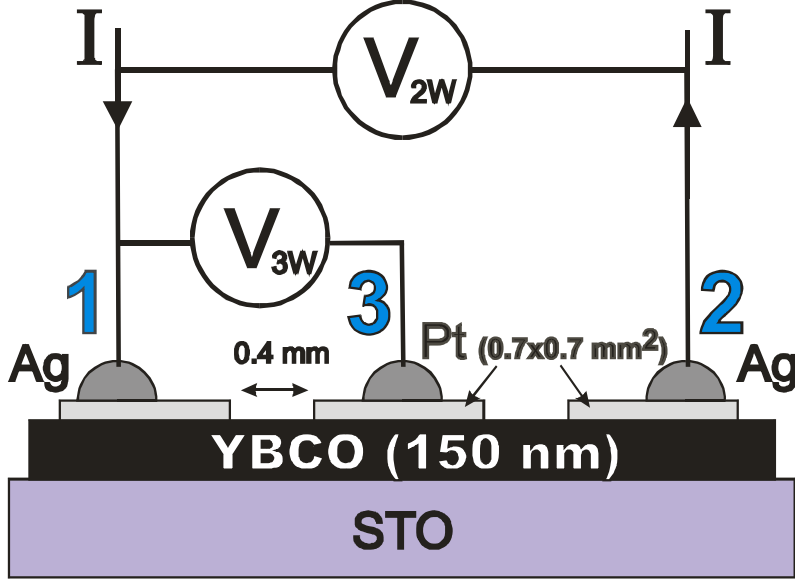


FIG. 3: Schematic of the studied Pt-YBCO_{7- δ} devices, showing the implemented electrical contacts distribution and the employed 2W and 3W setups.

at each step. Once an RS occurred, the experiment was terminated at that point and for all further temperatures. Thus, the study was restricted to IV curves that did not exhibit RS throughout the entire temperature range.

III. RESULTS AND DISCUSSION

In Figs. 4 and 5, the constant preservation of remanent resistance R_{rem} and the IV characteristics for all studied Pt-YBCO_{7- δ} interfaces at 290 K, within the utilized write voltage range are displayed, respectively.

The Pt-YBCO_{7- δ} devices exhibit distinct conduction levels, with nearly 3 orders of magnitude difference between the one based on the most oxygenated YBCO (S1) and the most deoxygenated (S4). The “safe” voltage and temperature range—*i.e.*, without causing a RS that could alter YBCO’s oxygen distribution—was highly variable across the samples, generally featuring a non-monotonic voltage scale, which was significantly reduced for the most conductive one (S1). Concerning the temperature range, the minimum value progressively increased as the samples became less conductive, severely limiting the range for S4.

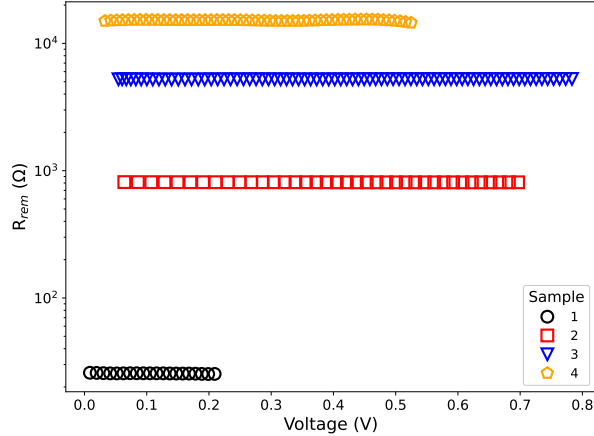


FIG. 4: Remanent resistance (R_{rem}) as a function of write voltage (V). Since no dependency is observed, we are confident that the resistive state of the interfaces was not altered during the study of the IV characteristics.

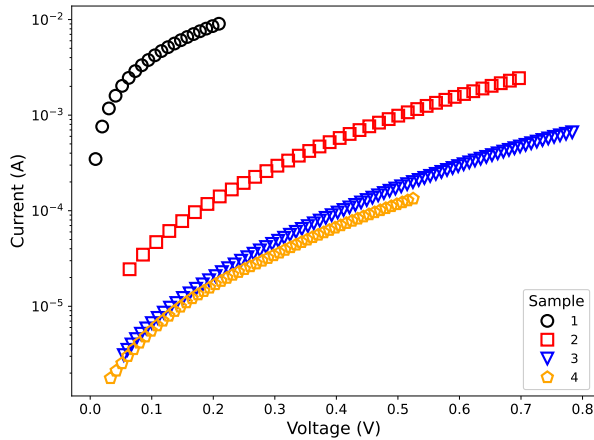


FIG. 5: Comparison of the IV characteristics of samples 1-4 at 290 K, within a limited range of voltages and currents to prevent resistive changes that could alter the original oxygen content in the vicinity of the contacts.

It can be observed that the functional dependence of the IV curves varies for each interface. To highlight these differences more effectively, the graphical representation of the power exponent $\gamma = d\ln(I)/d\ln(V)$ plotted against $V^{1/2}$, shown in Fig. 6, can be employed.²⁵ This method has proven highly valuable in identifying different transport mechanisms when multiple mechanisms contribute to electric transport.^{26–28} Distinct degrees of non-linearity are visible, consistent with already mentioned existence of diverse conduction

mechanisms, typically observed in metal-YBCO junctions, whose circuit representation, including a PF non-linear element, is depicted in Fig. 1.

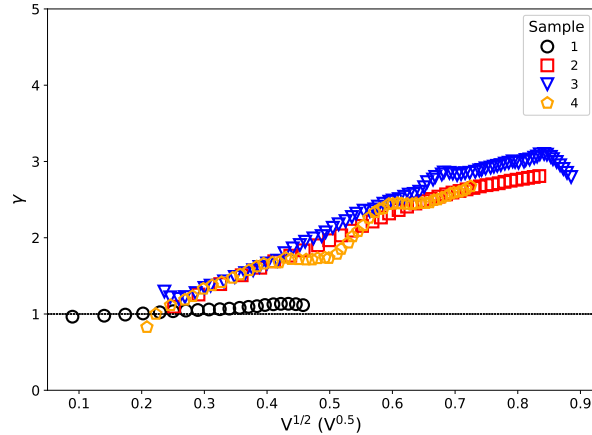


FIG. 6: Comparison of the parameter γ obtained for S1 to S4 at 290 K. A complex behavior is observed indicating the simultaneous existence of different conduction mechanisms, marked by both the varying degree of non-linearity ($\gamma > 1$) and the existence of ohmic processes, both in parallel ($\gamma \simeq 1$ at low voltages) and in series (maximum in γ for the highest voltages).

Fig. 7 illustrates the temperature sensitivity of the IV characteristics for S2, measured under both the 2W and 3W configurations. Similar results were obtained for the other samples. The electrical conductivity is observed to increase with rising temperature. A subtle rectification is noted but will be disregarded in the modeling process to maintain a straightforward and convenient description. Quantitative analysis will concentrate on the outcomes from the 3W configuration for all samples, ensuring a measurement solely of the contribution from one of the Pt-YBCO_{7- δ} interfaces rather than both.

Based on prior findings which indicated that the equivalent circuit shown in Fig. 1 is the optimal representation of the Pt-YBCO_{7- δ} interface^{14,29}, we can describe its DC electrical behavior using the following equations^{30,31}:

$$I_{PF}(V_{PF}) = A V_{PF} \exp \left[C \sqrt{V_{PF}} \right], \quad (1)$$

$$A = A_{PF} \exp \left[\frac{-\phi_T}{T} \right], \quad (2)$$

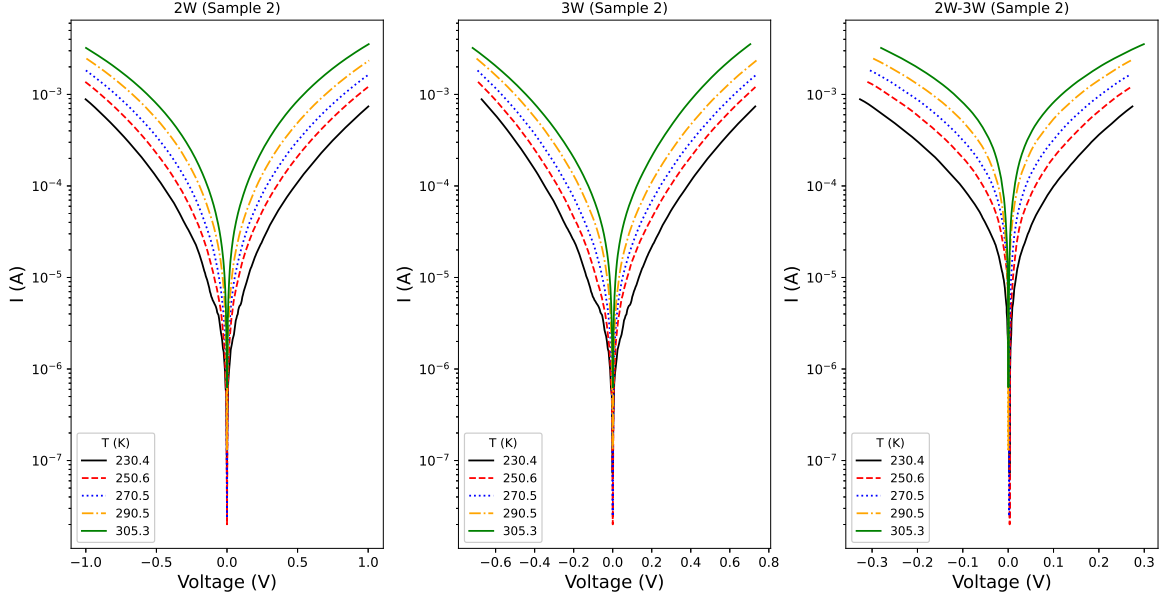


FIG. 7: IV characteristics as a function of temperature measured using either 2W (2 Pt-YBCO interfaces) or 3W (1st Pt-YBCO interface) configurations for S2. The 2W-3W is the mathematical difference of these measurements, indicating the IV dependence of the 2nd interface, not measured within the 3W configuration. Not appreciable rectification effects are observed, besides a small voltage asymmetry between the 3W and the 2W-3W measurements, which may be associated with the overall resistance of the external Cu-Ag-Pt pads.

$$A_{PF} = \frac{S}{d} q \mu (N_C N_D)^{1/2}, \quad (3)$$

$$C = \frac{q^{3/2}}{k_B T (\pi \epsilon' \epsilon_0 d)^{1/2}}, \quad (4)$$

where I_{PF} and V_{PF} are the current and the voltage across the PF element, respectively. S is the cross section area of the conducting path, q the electron's charge, μ the electronic drift mobility, N_C and N_D the density of states in the conduction band and the donor density, respectively. ϕ_T is the trap energy level (in K), k_B the Boltzmann constant, ϵ' the real part of the relative dielectric constant of the oxide, ϵ_0 the permittivity of vacuum and d the distance associated with the voltage drop V_{PF} . Notice that d may not necessarily be equivalent to the distance between the voltage contacts. As $V_{PF} = V - IR_s$ and $I = I_{PF} + I_{Rp}$, where R_s and R_p are the series and the parallel resistances, respectively, then:

$$I = A(V - I R_s) \exp \left[C \sqrt{V - I R_s} \right] + \frac{V - I R_s}{R_p}. \quad (5)$$

Equation 5 is an implicit equation requiring numerical solution for fitting the experimental data. For this purpose, we arbitrarily choose the IV data with positive V values and we applied an optimization technique that involved a generalized reduced gradient method for the A and C parameters, along with a 'brute force' variation of the R_p and R_s parameters. Testing different initial values for these parameters allowed us to identify the solution with the lowest residuals. We verified that the obtained parameters for this solution (within a 10% range) consistently minimized residuals when fitting the data from the negative V quadrant.

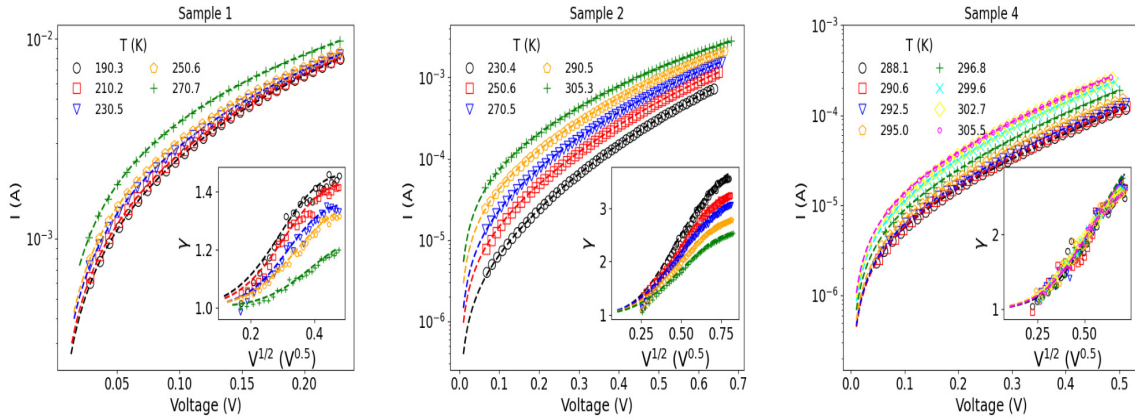


FIG. 8: IV characteristics at different temperatures for S1, S2 and S4. The dashed lines are fits using the electric circuit model of Fig. 1 associated with Eq. 5. The inset shows the dependence of γ on $V^{1/2}$ at different temperatures for the experimental data, where the dashed lines represent the obtained γ for the fitting IV curves, also showing an excellent agreement. Similar results were obtained for S3 (see Supplementary Material).

As can be observed in Fig. 8, the experimental IV characteristics for S1, S2 and S4 are very well reproduced by the theoretical representation of the proposed circuit model (Fig. 1 and Eq. 5), respectively. The quality of the fits can also be appreciated in the representation of the γ curves, shown as an inset in Fig. 8). A small deviation can be observed at low currents and voltages, likely attributed to the presence of minimal thermoelectric voltages

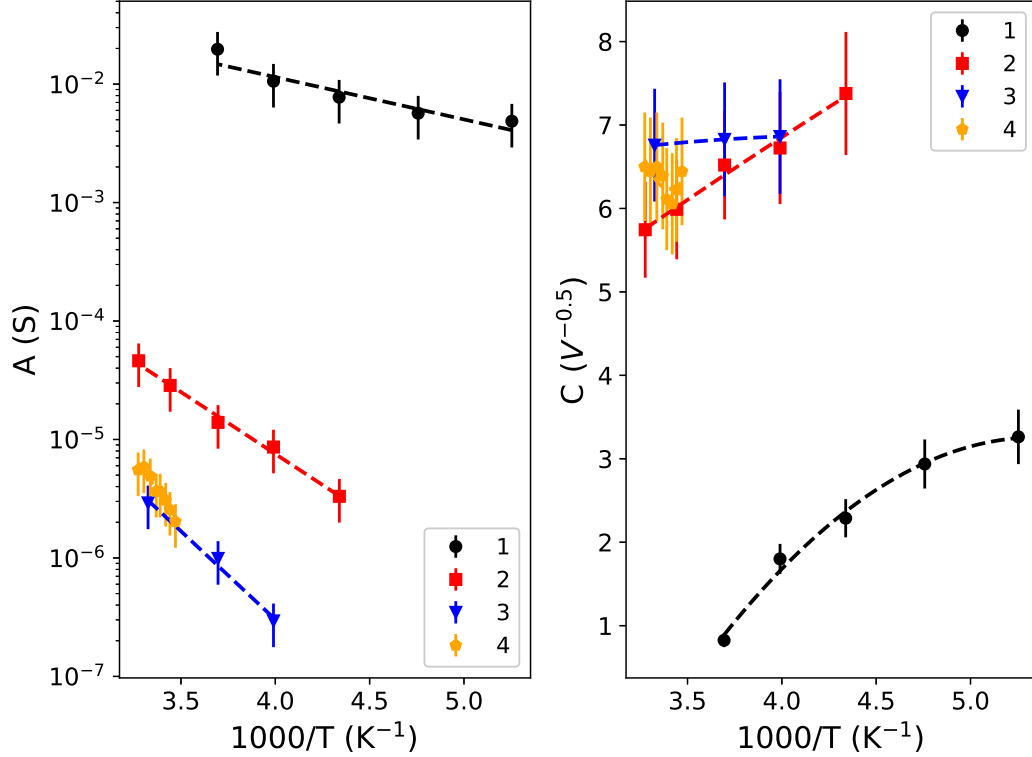


FIG. 9: The obtained A and C Poole-Frenkel parameters after fitting the IV characteristics as a function of temperature for all the samples. Dashed lines for the A parameter are fits using Eq. 2 while they are guides to the eye for C parameter.

at the interfaces as well as well as the minor rectifying effects already mentioned. Similar results were obtained for S3 (see Supplementary Material).

The parameters of the best fits can be observed in Figs.9 and Fig.10. For parameter A , the expected dependence according to Eq.2 is obtained, confirming that the term A_{PF} remains essentially temperature-independent within the studied range and varies with the oxygen content of YBCO. Regarding parameter C , the only sample showing consistent behavior with Eq.4 is S2. This is strongly linked to the temperature dependence that the ϵ' associated with this PF-type conduction zone may exhibit. This indicates that S2 presents a temperature-independent ϵ' , while this is not the case for the other samples.

The behavior of the parallel resistance, R_p (see Fig. 10), is consistent with previous results^{14,29}, where we observed that it can be considered as an ohmic leakage channel. It corresponds to a semiconductor-type conduction, more specifically that associated with disorder (variable range hopping). In general, it is observed that with greater deoxygenation,

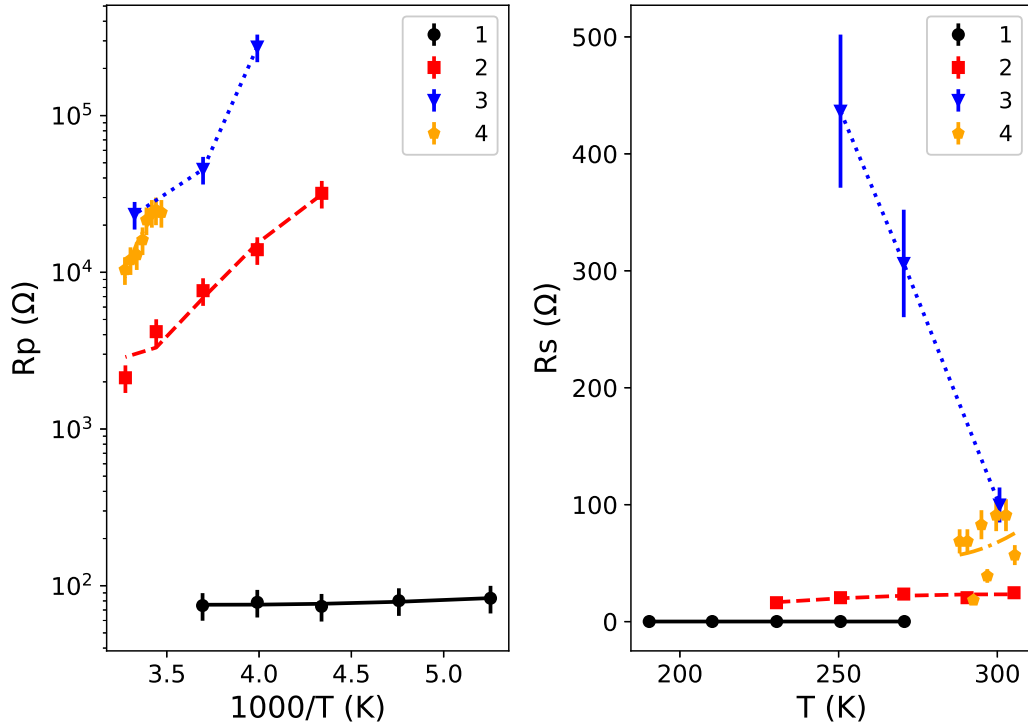


FIG. 10: The obtained parallel (R_p) and series resistance (R_s) after fitting the IV characteristics as a function of temperature for all the samples. Lines are guides to the eye.

both the resistance value and its slope (vs. $1/T$) increase. On the other hand, the series resistance, R_s , is metallic-like for the more oxygenated samples (S1 and S2) and semiconducting for S3. The behavior of S4 is not quite clear, probably as a result of the high noise level (low currents) and the constrained temperature range studied.

Finally, the dependence of parameters A_{PF} and ϕ_T on δ , associated with Eq.2, is depicted in Fig. 11. It is observed that A_{PF} exhibits a non-monotonic behavior and a sharp rise for $\delta = 0.56$, whereas ϕ_T shows a logarithmic-type increase. We understand that the complex response of the parameter A_{PF} is associated with its multiple dependencies, as it relates both to electronic parameters (donor density, density of states in the conduction band, carrier mobility) and geometric parameters (the conduction surface and the thickness of the interfacial region, see Eq. 3). This competition among parameters complicates the inference of the expected behavior with varying δ . However, we understand that the significant increase observed at the highest δ likely indicates a substantial shift in detrapped carrier mobility or changes in geometric factors, such as an expanded effective conduction area or

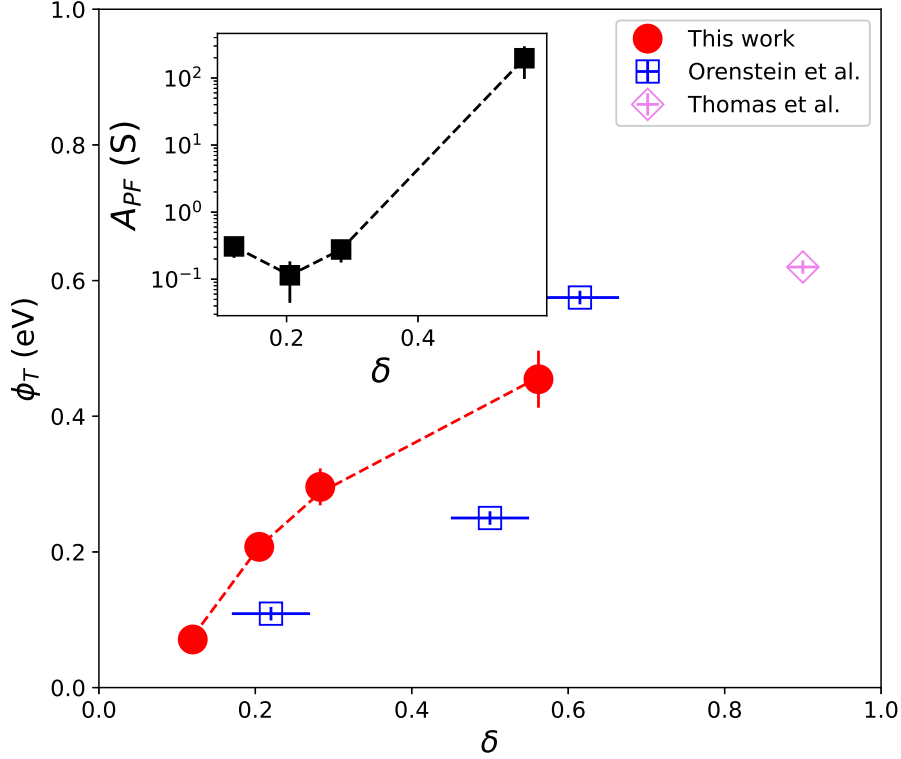


FIG. 11: Oxygen deficiency (δ) dependence of the trap energy [$\phi_T(\delta)$] (red solid circles). $E_T(\delta)$ extracted from optical conductivity measurements from Orenstein et. al. (ref.³²) and Thomas et al. (ref.³³) (blue squares and violet diamond, respectively). The inset shows the δ dependence of the Poole-Frenkel pre-factor [$A_{PF}(\delta)$]. Dashed lines are guides to the eye.

a reduced interfacial zone. The dependence of ϕ_T on δ confirms that the trap potential well affecting PF conduction deepens as the concentration of oxygen vacancies in YBCO increases. This observation validates the role of oxygen vacancies in generating traps for charge carriers traveling through YBCO.

The established empirical $\phi_T(\delta)$ relation can be used to infer the oxygen content from electrical transport measurements. In previous work¹⁴, it was shown that ϕ_T could be altered by applying either higher amplitude pulses or a greater number of pulses of the same amplitude. After applying pulses that caused a 200% increase in the initial resistance of an Au-YBCO device, ϕ_T increased from approximately 0.06 eV to 0.11 eV. From Fig. 11 we can estimate that this represents a local change in delta from $\simeq 0.11$ to 0.13. These values are in agreement with the studies conducted in that work on the temperature dependence

of the resistance of those interfaces, as no signs of electronic localization (VRH) were observed, which would have been expected for higher values of δ . This consistency highlights the viability of employing electrical transport as a tool to assess the oxygen content in the interfacial zone of the metal-YBCO junction.

To better understand the implications of the observed $\phi_T(\delta)$ dependence, we might examine studies involving optical conductivity, which has played a key role in disentangling the complexities of electronic band structures and basic excitations. Indeed, by conducting optical reflectivity, ellipsometry, and Raman scattering studies on YBCO_{6+x} ($0 \leq x \leq 1$) samples, Cooper et al.³⁴ compared findings from twinned YBCO single crystals to those single-domain, as well as from BSCCO crystals (which do not contain CuO chains). This allowed them to distinguish the contributions to optical conductivity arising from both CuO₂ plane transitions and CuO chains. One of their key observations was that in samples where $x < 0.8$ (i.e. $\delta > 0.2$), a mid-infrared peak is detected in the electrical conductivity, shifting towards lower energies as oxygen vacancies are reduced. This absorption, which is solely attributed to the CuO chains where the oxygen vacancies are located, leads to a deviation from the observed low-frequency dependence ($\sigma \sim \omega^{-1}$), potentially indicating the presence of an electronic band associated with the vacancies. In other words, it seems reasonable to associate this region of increased absorption with the set of energies required to ionize an impurity charge (E_I)³⁵, that is, to extract a charge carrier from the potential well associated with the oxygen vacancy and promote it to the conduction band or to similar energy bands.

Thomas et al. (ref.³³) analyzed the optical conductivity of several lightly doped cuprates (including YBCO_x with $x \simeq 6.1$), revealing the presence of two peaks for energies below 1 eV. The plausibility of associating the higher energy peak with E_I was discussed. Similarly, we have extracted from ref.³² the energies of the maxima in $\sigma(\omega)$ for YBCO_{7- δ} samples with $30 \text{ K} \leq T_c \leq 80 \text{ K}$. We were able to correlate T_c with δ based on studies that defined T_c similarly (onset of the magnetization curve at low field).^{2,36} A detailed description of the procedure we applied can be found in the Supplementary Information section. These derived $E_I(\delta)$ points have been added to Fig. 11, showing a strong correlation with $\phi_T(\delta)$. This strengthens the initial interpretation regarding the origin of this optical conductivity peak as an ionization energy.

IV. CONCLUSIONS

We have measured the electrical transport across Pt-YBa₂Cu₃O_{7- δ} ($0.12 \leq \delta \leq 0.56$) interfaces at various temperatures. Results were analyzed by considering a circuit model, previously demonstrated to be effective in describing transport in optimally doped metal-YBCO junctions. The model features two interfacial component –a PF emission-based element in parallel with a resistor– in series with a bulk resistance (R_s) considerably smaller than R_p , highlighting the dominance of interfacial effects in transport properties. Since Pt electrodes are chemically inert with respect to YBCO, the observed PF emission can be attributed to intrinsic YBCO properties linked to oxygen vacancies. Importantly, the microscopic parameters governing PF emission–notably the trap energy–demonstrated a systematic dependence on oxygen content. As δ increased, so did the energy of the potential wells, a trend that correlates strongly with a peak identified in optical conductivity studies. This reinforces the proposed relationship between oxygen vacancies and the ionization energy of charges localized within impurity bands, offering deeper insights into the microscopic transport mechanisms in oxygen-depleted YBCO.

V. ACKNOWLEDGEMENTS

We acknowledge very useful discussions with Dr. V. Ferrari and Dr. J. Dilson, as well as financial support by CONICET Grant PIP 11220200101300CO and UBACyT 20020220200062BA (2023-2025). Jenny and Antti Wihuri Foundation is also acknowledged for financial support.

VI. SUPPLEMENTARY INFORMATION:

A. Oxygen deficiency determination

1. The intensity ratio between the XRD peaks (005) and (004), $I(005)/I(004)$, is calculated from the peak areas shown on the left-hand side of Fig. 12. This intensity ratio is also presented in the table at the bottom right.
2. The relationship between the oxygen deficiency, δ , and the intensity ratio $I(005)/I(004)$ is derived from Ye's and Nakamura's paper²⁴, as shown in the figure inset. The data points in the inset are taken from the paper, and we have fitted a third-order polynomial function to describe this relationship.
3. By inputting the measured intensity ratios into the polynomial function, the corresponding oxygen deficiencies (δ) can be calculated. These values are also shown in the table at the bottom right.
4. The measured critical temperature values can then be plotted as a function of the oxygen deficiency, as presented in Fig. 2 (main text).

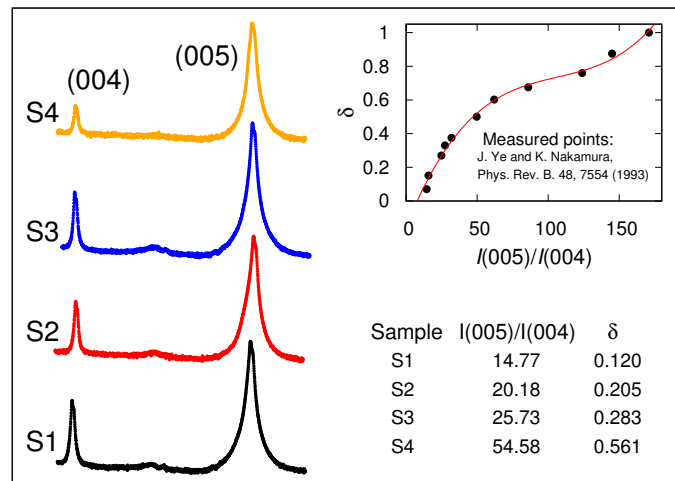


FIG. 12: XRD of S1-S2-S3-S4 focused on the 2θ (005) and (004) peaks (left side). The δ dependence on the $I(005)/I(004)$ peak intensity ratio, from ref.²⁴ (upperside right) and the table with the obtained values (downside right).

B. IV characteristics of S3

The IV characteristics as well as the γ parameter for S3, not included in the main text for simplicity, are shown in Fig. 13.

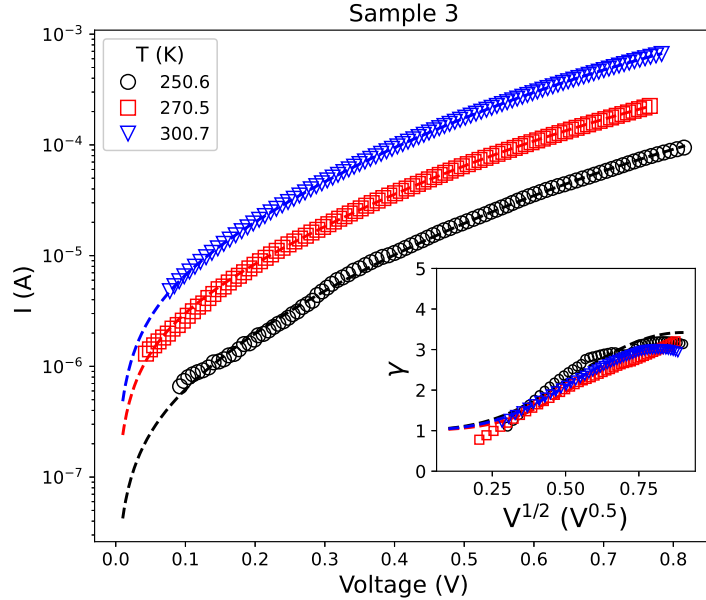


FIG. 13: IV characteristics at different temperatures for S3. The dashed lines are fits using the electric circuit model of Fig. 1 associated with Eq. 5. The inset shows the dependence of γ on $V^{1/2}$ at different temperatures for the experimental data, where the dashed lines represent the obtained γ for the fitting IV curves, also showing a good agreement.

C. $E_I(\delta)$ extracted from Orenstein et al.³²

Thomas et al.³³ studied the optical conductivity of several lightly doped semiconductors derived from cuprates, among which $\text{YBa}_2\text{Cu}_3\text{O}_{6.1}$ was included. Their analysis revealed that for energies lower than 1.25 eV, all spectra shared common characteristics, most prominently two peaks attributed to the energies labeled E_J and E_I . These energies were determined through fits employing Lorentzian functions. The authors interpreted the higher-energy peak (E_I) as analogous to an impurity band and suggested that it might represent the energy required for a transition from a bound state to the continuum.

To analyze the possibility that E_I could correspond to the energy of PF traps (ϕ_{PF}),

we extracted the tabulated value from this publication ($\delta = 0.9$, $E_I = 0.62$ eV). To add additional data points corresponding to more doped samples, which have fewer oxygen vacancies, we referred to the work of Orenstein *et al.*³², where the optical conductivity as a function of energy is shown (see Fig. 5). Specifically, we digitized the curves corresponding to samples with superconducting transition temperatures of $T_c = 80$ K, 50 K, and 30 K, all of which displayed a peak in the energy region < 1.25 eV. Since these samples are more doped than the one studied in ref[xx], they exhibit Drude-type absorption for $\omega \rightarrow 0$, which could obscure E_J and possibly E_I in the $T_c = 90$ K sample. Figure S3 shows the digitized data along with the fitted peaks, whose values were used to estimate E_I . Uncertainties were associated with the peak width and were increased due to the noise introduced during digitization.

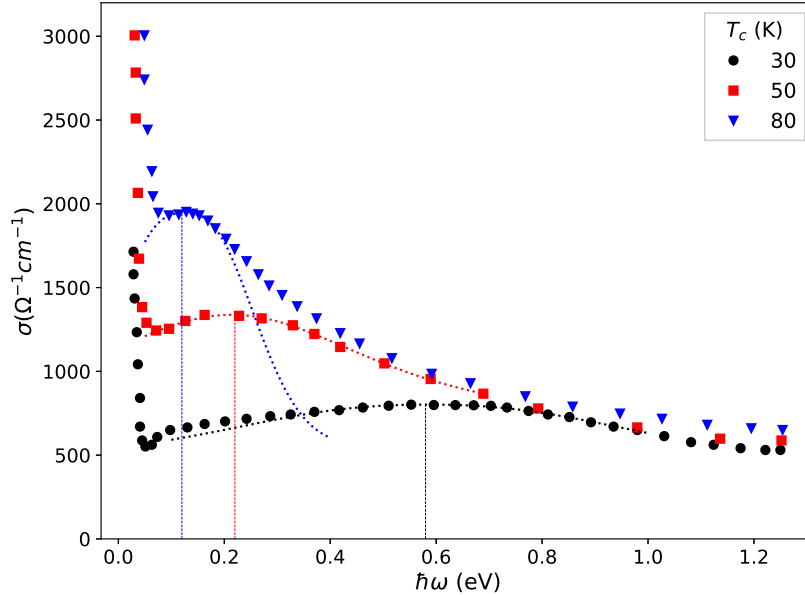


FIG. 14: Optical conductivity as a function of the energy. The data points result from the partial digitization of curves corresponding to samples with $T_c = 30$ K, 50 K, and 80 K, as presented in Fig. 3 of the work by Orenstein *et al.*⁽³²⁾ The peak energies, determined through optimal fitting with a Pseudo-Voigt function to address the asymmetry of the observed peaks (dashed curves), are 0.12 eV, 0.22 eV, and 0.58 eV, respectively.

Additionally, since the authors provide the superconducting transition temperature (T_c) of the studied samples rather than their δ values, we relied on the works of Cava *et al.*³⁶ and Jorgensen *et al.*², where the δ value was correlated with the T_c of $YBCO_{7-\delta}$ crystals using

the same criterion to determine T_c . By digitizing Figures 1 (Cava *et al.*) and 3 (Jorgensen *et al.*), we obtained Figure S4. It illustrates how we estimated the δ values for the samples studied by Orenstein *et al.*.

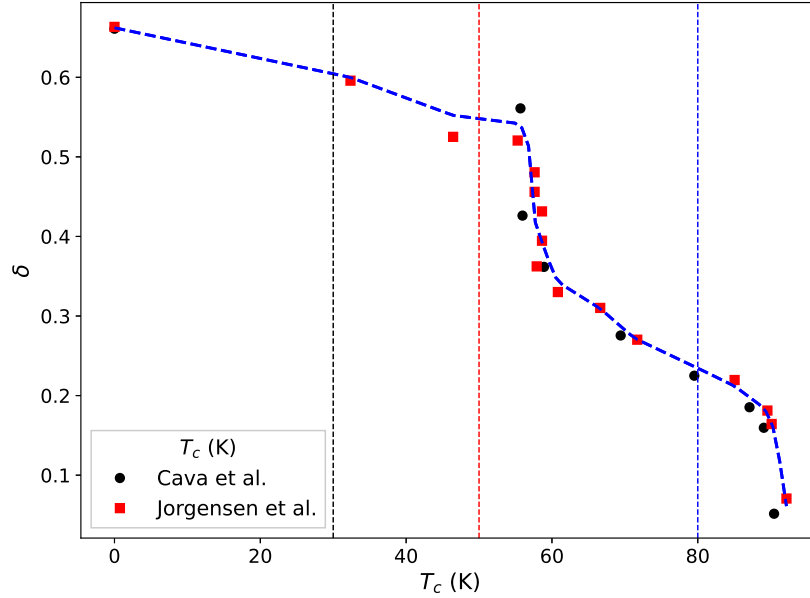


FIG. 15: Oxygen vacancy content as a function of T_c determined as the onset of magnetization measurements at low magnetic field (5 Oe). The data points were extracted by partially digitizing the original figures from Cava *et al.*³⁶ and Jorgensen *et al.*². The dashed blue line correspond to the mean interpolated curve. Dashed vertical lines indicate the T_c values (determined using the same method) of some samples from the study by Orenstein *et al.*³² (30 K, 50 K, and 80 K). The average δ values obtained are 0.22, 0.55, and 0.61, respectively.

-
- * corresponding author (acha@df.uba.ar)
- ¹ J. L. Tallon, Ybco 1, in: A. B. David A. Cardwell, David C. Larbalestier (Ed.), Handbook of Superconductivity, Taylor and Francis Group, Boca Raton, 2023, pp. 2–40, chapter C1.
 - ² J. D. Jorgensen, B. W. Veal, A. P. Paulikas, L. J. Nowicki, G. W. Crabtree, H. Claus, W. K. Kwok, Structural properties of oxygen-deficient $YBa_2Cu_3O_{7-\delta}$, Phys. Rev. B 41 (1990) 1863–1877. doi:10.1103/PhysRevB.41.1863.
URL <https://link.aps.org/doi/10.1103/PhysRevB.41.1863>
 - ³ M. J. Rozenberg, M. J. Sánchez, R. Weht, C. Acha, F. Gomez-Marlasca, P. Levy, Mechanism for bipolar resistive switching in transition-metal oxides, Phys. Rev. B 81 (2010) 115101.
 - ⁴ A. Schulman, M. J. Rozenberg, C. Acha, Anomalous time relaxation of the nonvolatile resistive state in bipolar resistive-switching oxide-based memories, Phys. Rev. B 86 (2012) 104426.
 - ⁵ T. Plecenik, M. Tomasek, M. Belogolovskii, M. Truchl, M. Gregor, J. Noskovic, M. Zahoran, T. Roch, I. Boylo, M. Spankova, S. Chromik, P. Kus, A. Plecenik, Effect of crystallographic anisotropy on the resistance switching phenomenon in perovskites, J. Appl. Phys. 111 (2012) 056106.
 - ⁶ C. Acha, M. J. Rozenberg, Non-volatile resistive switching in the dielectric superconductor $YBa_2Cu_3O_{7-\delta}$, J. Phys.: Condens. Matter 21 (2009) 045702.
 - ⁷ C. Acha, Electric pulse-induced resistive switching in ceramic $YBa_2Cu_3O_{7-\delta}/Au$ interfaces, Physica B 404 (2009) 2746.
 - ⁸ A. Plecenik, M. Tomasek, T. Plecenik, M. Truchly, J. Noskovic, M. Zahoran, T. Rocha, M. Belogolovskii, M. Spankova, S. Chromik, P. Kus, Studies of resistance switching effects in metal/ $YBa_2Cu_3O_{7-x}$ interface junctions, Appl. Surface Science 256 (2010) 5684.
 - ⁹ C. Acha, Dynamical behaviour of the resistive switching in ceramic YBCO/metal interfaces, J.Phys.D: Appl.Phys. 44 (2011) 345301.
 - ¹⁰ A. Schulman, C. Acha, Cyclic electric field stress on bipolar resistive switching devices, J. Appl. Phys. 114 (2013) 243706.
 - ¹¹ A. Schulman, C. Acha, MRS Proceedings 1337 (2011) q10–07.
 - ¹² A. Palau, A. Fernandez-Rodriguez, J. C. Gonzalez-Rosillo, X. Granados, M. Coll, B. Bozzo, R. Ortega-Hernandez, J. Suñé, N. Mestres, X. Obradors, T. Puig, Electrochemical tuning of

- metal insulator transition and non-volatile resistive switching in superconducting films, *ACS Applied Materials & Interfaces* 10 (36) (2018) 30522–30531.
- ¹³ J. Alcalà, A. Fernández-Rodríguez, T. Güntel, A. Barrera, M. Cabero, J. Gazquez, L. Balcells, N. Mestres, A. Palau, Tuning the superconducting performance of $\text{YBa}_2\text{Cu}_3\text{O}_{7-\delta}$ films through field-induced oxygen doping, *Scientific Reports* 14 (2024) 1939. doi:10.1038/s41598-024-52051-1.
- ¹⁴ A. Schulman, L. F. Lanosa, C. Acha, Poole-frenkel effect and variable-range hopping conduction in metal/YBCO resistive switching devices, *Journal of Applied Physics* 118 (2015) 044511.
- ¹⁵ J. Waśkiewicz, J. Golebiowski, Resistive memory physical mechanism in a thin-film $\text{Ag}/\text{YBa}_2\text{Cu}_3\text{O}_{7-x}/\text{Ag}$ structure, *Przeglad Elektrotechniczny* 91 (2015) 313–317.
- ¹⁶ M. Truchly, T. Plecenik, E. Zhitlukhina, M. Belogolovskii, M. Dvoranova, P. Kus, A. Plecenik, Inverse polarity of the resistive switching effect and strong inhomogeneity in nanoscale ybco-metal contacts, *Journal of Applied Physics* 120 (18) (2016) 185302. doi:10.1063/1.4967392.
- ¹⁷ J. Waśkiewicz, Measurement of the thickness of the oxygen-depleted layer in the $\text{Ag}/\text{YBa}_2\text{Cu}_3\text{O}_{7-x}/\text{Ag}$ structures of the electro-resistance memory, *Przeglad Elektrotechniczny* 94 (2018) 99–103.
- ¹⁸ N. A. Tulina, A. N. Rossolenko, I. M. Shmytko, A. A. Ivanov, V. V. Sirotkin, I. Y. Borisenko, V. A. Tulin, Properties of percolation channels in planar memristive structures based on epitaxial films of a $\text{YBa}_2\text{Cu}_3\text{O}_{7-\delta}$ high temperature superconductor, *Superconductor Science and Technology* 32 (1) (2018) 015003. doi:10.1088/1361-6668/aae966.
- ¹⁹ S. M. Sze, K. K. Ng, *Physics of Semiconductor Devices*, John Wiley & Sons, 2007.
- ²⁰ A. Matsushita, T. Oguchi, K. Kimura, T. Matsumoto, T. Hatano, K. Ogawa, S. Takayanagi, *Jap. J. Appl. Phys.* 26 (1987) L1953.
- ²¹ H. Palonen, H. Huhtinen, M. Shakhov, P. Paturi, Electron mass anisotropy of BaZrO_3 doped YBCO thin films in pulsed magnetic fields up to 30 T, *Superconductor Science and Technology* 26 (2013) 045003. doi:10.1088/0953-2048/26/4/045003.
- ²² M. M. Aye, E. Rivasto, M. Khan, H. Rijckaert, E. Salojärvi, C. Haalisto, E. Mäkilä, H. Palonen, H. Huhtinen, I. Van Driessche, P. Paturi, Control of the nanosized defect network in superconducting thin films by target grain size, *Scientific Reports* 11 (03 2021). doi:10.1038/s41598-021-85304-4.
- ²³ M. Khan, E. Rivasto, H. Rijckaert, Y. Zhao, M. Liedke, M. Butterling, A. Wagner, I. Van Driess-

- che, H. Huhtinen, P. Paturi, Strongly enhanced growth of high-temperature superconducting films on an advanced metallic template, *Crystal Growth & Design* 22 (03 2022). doi: 10.1021/acs.cgd.1c01101.
- ²⁴ J. Ye, K. Nakamura, Quantitative structure analyses of $\text{YBa}_2\text{Cu}_3\text{O}_{7-\delta}$ thin films: Determination of oxygen content from x-ray-diffraction patterns, *Phys. Rev. B* 48 (1993) 7554–7564. doi: 10.1103/PhysRevB.48.7554.
- ²⁵ C. Acha, Graphical analysis of current-voltage characteristics in memristive interfaces, *Journal of Applied Physics* 121 (13) (2017) 134502.
- ²⁶ C. Acha, A. Schulman, M. Boudard, K. Daoudi, T. Tsuchiya, Transport mechanism through metal-cobaltite interfaces, *Applied Physics Letters* 109 (2016) 011603.
- ²⁷ W. R. Acevedo, C. Acha, M. J. Sánchez, P. Levy, D. Rubi, Origin of multistate resistive switching in Ti/manganite/ SiO_x /Si heterostructures, *Applied Physics Letters* 110 (2017) 053501.
- ²⁸ N. Ghenzi, M. Barella, D. Rubi, C. Acha, Adaptive threshold in TiO_2 -based synapses, *Journal of Physics D: Applied Physics* 52 (12) (2019) 125401. doi:10.1088/1361-6463/aafdf3.
- ²⁹ L. F. Lanosa, H. Huhtinen, P. Paturi, C. Acha, Electrical conduction mechanisms of metal / high- T_c superconductor (YBCO) interfaces, *Journal of Physics: Condensed Matter* 32 (17) (2020) 175001.
- ³⁰ R. M. Hill, Poole-frenkel conduction in amorphous solids, *The Philosophical Magazine: A Journal of Theoretical Experimental and Applied Physics* 23 (181) (1971) 59–86. doi: 10.1080/14786437108216365.
- ³¹ W. Vollmann, Poole-Frenkel conduction in insulators of large impurity densities, *Physica Status Solidi (a)* 22 (1) (1974) 195–203. doi:10.1002/pssa.2210220122.
- ³² J. Orenstein, G. A. Thomas, A. J. Millis, S. L. Cooper, D. H. Rapkine, T. Timusk, L. F. Schneemeyer, J. V. Waszczak, Frequency- and temperature-dependent conductivity in $\text{YBa}_2\text{Cu}_3\text{O}_{7-\delta}$ crystals, *Phys. Rev. B* 42 (1990) 6342–6362. doi:10.1103/PhysRevB.42.6342.
- ³³ G. A. Thomas, D. H. Rapkine, S. L. Cooper, S.-W. Cheong, A. S. Cooper, L. F. Schneemeyer, J. V. Waszczak, Optical excitations of a few charges in cuprates, *Phys. Rev. B* 45 (1992) 2474–2479. doi:10.1103/PhysRevB.45.2474.
- ³⁴ S. L. Cooper, D. Reznik, A. Kotz, M. A. Karlow, R. Liu, M. V. Klein, W. C. Lee, J. Giapintzakis, D. M. Ginsberg, B. W. Veal, A. P. Paulikas, Optical studies of the a-, b-, and c-axis charge dynamics in $\text{YBa}_2\text{Cu}_3\text{O}_{6+x}$, *Phys. Rev. B* 47 (1993) 8233–8248. doi:10.1103/PhysRevB.47.

8233.

³⁵ N. F. Mott, Metal-insulator transitions, Taylor & Francis, 1990.

³⁶ R. Cava, A. Hewat, E. Hewat, B. Batlogg, M. Marezio, K. Rabe, J. Krajewski, W. P. Jr., L. R. Jr., Physica C: Superconductivity 165 (1990) 419.